Progress In Electromagnetics Research M, Vol. 97, 201–213, 2020

A Study on Electromagnetic Field and Force for Magnetic Micro-Robots Applications

Chuan Qu, Yong-Chen Pei*, Long Xu, Zheng-Rong Xia, and Qing-Yuan Xin

Abstract—Magnetic micro-robots are used widely in a narrow space, such as internal inspections and desilting of slender pipelines, minimal- or non-invasive diagnoses, and treatments of various human diseases in blood vessels, and micro-manipulations, micro-sensing fields. Magnetic micro-robots are usually driven by several electromagnetic coils. It is essential to understand the magnetic field and magnetic forces acting on micro-robots to drive the magnetic micro-robots more effectively. In this paper, the finite element method is applied to simulate the magnetic field generated by a coil assembly. Moreover, a three-dimensional magnetic force simulation is also performed to reveal the magnetic forces acting on a cylindrical magnetic micro-robot. Experimental measurements validate the simulated results. A Hall sensor is used to measure the magnetic field along the coil assembly's axial and radial direction. The micro-robot is glued to a connecting rod, fixing a force sensor to measure the magnetic forces acting on it. The measured results are in good accordance with the simulated ones, which prove the validity of the simulation. The results from this study show potential to provide a reference to magnetic micro-robot applications.

1. INTRODUCTION

Nowadays, more and more researchers focus on micro-robots. Various methods have been suggested to drive micro-robots, such as electric field, magnetic field, light energy, ultrasonic field, polymer actuators, and chemical reaction [1–3]. Compared with the mentioned methods, magnetic actuation is a typical method of driving micro-robots remotely, which has the advantages of rapid response, high control accuracy, and high compatibility [4–6]. Nelson et al. [7] and Sitti et al. [8] published a review to analyze the types of micro-robots and predicted the application prospect, respectively. In particular, wireless magnetic micro-robots can be applied to micromanipulations, such as assembling micro-parts to build complex micro-mechanical systems, micro-objects transporting in a limited space, and even implanting human bodies to perform drug delivery and biomanipulation of single cell tasks in the biomedicine field [9–14].

To achieve the applications mentioned above, the magnetic micro-robots must be driven and controlled accurately. In general, permanent magnets and electromagnetic coils can generate a magnetic field to use as magnetic driving sources; the former can generate a higher magnetic field, while the latter performs better in controlling electromagnetic field strength and direction. Besides, using coils to control magnetic micro-robots' trajectory is more flexible by adjusting the input voltages or currents of coils. Therefore, the electromagnetic coil could work better in this respect. To date, several magnetic micro-robots and corresponding driving devices have been developed [15–18]. For instance, Jeong et al. proposed a three-dimensional (3D) electromagnetic actuation (EMA) system to propel a micro-robot in blood vessels, consisting of a pair of stationary Helmholtz-Maxwell coils and a pair of rotational Helmholtz-Maxwell coils [19]. Choi et al. proposed two static EMA systems. One includes two pairs

Received 30 July 2020, Accepted 14 October 2020, Scheduled 21 October 2020
* Corresponding author: Yong-Chen Pei (yongchen_pei@hotmail.com).
The authors are with the Key Laboratory of CNC Equipment Reliability, Ministry of Education, School of Mechanical and Aerospace Engineering, Jilin University, Changchun, Jilin 130022, China.

of Helmholtz coils and one pair of Maxwell coils, and the other consists of two pairs of Helmholtz and Maxwell coils [20, 21]. Kee et al. proposed a quadrupole EMA system with movable magnetic cores and confirmed the developed system's effectiveness for driving micro-robots with various sizes [22].

Both soft magnetic materials (e.g., Fe, Ni, NiFe, FeSiB, MnZn) and hard magnetic materials (e.g., NdFeB, SmCo) can be utilized to fabricate micro-robots [23–26]. The former is characterized by high permeability and low coercivity ($H_{ci} < 10^3$ A/m), easily magnetized and demagnetized by external magnetic fields. The latter has much lower permeability but high coercivity ($H_{ci} > 10^4$ A/m) and large remnant magnetization [27]. In this paper, a permanent magnetic micro-cylinder acts as a micro-robot. In order to control the micro-robot precisely, it is crucial to characterize the magnetic field near the micro-robot [28] and understand the magnetic forces exerting on it [22, 29, 30].

Aforementioned EMA systems [19–21] present analogous structures consisted of several coils without iron cores, which are used to drive micro-robots by setting the voltages or currents in each coil [31, 32]. However, shortcomings are oversize and thermal effect because of many coil turns or a large current in the coils to generate a sufficient magnetic field and gradient for driving micro-robots. The coil with an iron core is a good method to increase the magnetic field and gradient. Thus this work aims to simulate the magnetic field generated by a coil assembly (a coil with an iron core) and the magnetic forces acting on a magnetic micro-robot. The simulation results are validated by experimental measurements. Simulation and measurement of the magnetic field and forces for the single coil assembly can contribute to novel EMA systems' optimal design to drive micro-robots more effectively. Furthermore, determine the working area where the magnetic micro-robot can reach and precisely control its movement.

The rest of this paper is organized as follows. The second section briefly introduces the single coil assembly. The third section simulates and measures the magnetic field generated by the coil assembly, including the axial and radial directions of the coil assembly. The fourth section simulates and measures the magnetic forces acting on the micro cylinder along the axial and radial directions of the coil assembly in the three dimensions. The final section of this paper summarizes the conclusions.

2. COIL ASSEMBLY

The schematic diagram of the single coil assembly is illustrated in Fig. 1. Its compositions mainly include a coil, an iron core, and plastic brackets, a fundamental component for developing new electromagnetic driving systems. Plastic brackets are used to limit the position of the coil. The iron core is made of electromagnetic pure iron material with a grade of DT4C, which exhibits excellent electromagnetic properties, such as low coercivity, high permeability, high-saturation magnetic induction, and no magnetic aging problem. The iron core can concentrate the coil's magnetic field and increase the magnetic field gradient, but further add to the complexity of the magnetic field. Consequently, the finite element method (FEM) is an effective method for the following magnetic field simulation.

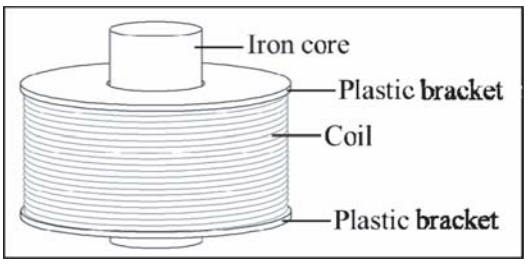

Figure 1. Schematic diagram of the coil assembly.

3. SIMULATION AND MEASUREMENT FOR THE ELECTROMAGNETIC FIELD

3.1. Electromagnetic Field Simulation

The magnetic field generated by the coil assembly is simulated in ANSYS Maxwell software. The parameters used in the simulation are listed in Table 1. In order to describe the magnetic field along

Table 1. Parameters used in the simulation.

Parameter	Value
Wire diameter of the coil, d_0	0.75 mm
Length of the coil, L_1	49 mm
Thickness of the coil, T	14.35 mm
Turn of the coil, N	1035
Resistance of the coil, R	6.9 Ω
Length of the core, L_2	99.5 mm
Diameter of the core, D	23 mm
Relative permeability of the core, μ_r	4000

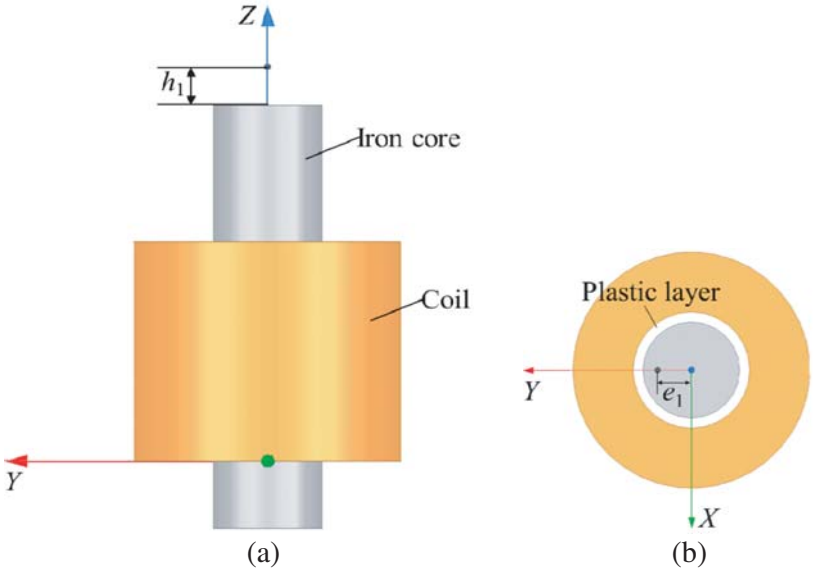

Figure 2. 3D model of the coil assembly. (a) Front view; (b) Top view.

the central axis and radial direction of the coil assembly, a 3D geometric model is constructed and shown in Fig. 2. The height between the magnetic field position and the iron core's upper surface is along the coil assembly axis, expressed by h_1; e_1 denotes the radial distance between the magnetic field position and the coil assembly's central axis.

The model is simplified as a section rotating around the symmetry axis due to the structure symmetry along the model's central axis (Z-axis). The two-dimensional (2D) simulation of the magnetic field is performed to improve the simulation speed. The face current $I_f = NU/R$ is applied to the coil, where U is the input voltage of the coil. The air domain's size is three times of the model's size. The balloon boundary condition is applied to the air domain, which is an infinite far boundary condition, and the magnetic field can cross this boundary. The mesh refinement can improve simulation accuracy, and the mesh statistics is shown in Table 2.

When the coil assembly's input voltage is 6 V, the 2D simulation model and magnetic flux lines of the coil assembly are shown in Fig. 3(a). The magnetic flux density (sometimes also called magnetic induction, it is a parameter representing the magnetic field) is shown in Fig. 3(b), which displays the maximum magnetic flux density in the position of the iron core corresponding to the coil middle position.

Figure 4 shows the effect of input voltage U on magnetic flux density B_z along the coil assembly's axial and radial directions. Fig. 4(a) indicates that the magnetic flux density B_z along the central axis of the coil assembly and at the same height h_1 is proportional to the input voltage. At a given voltage,

Table 2. Mesh statistics.

Model	Mesh type	Number of elements	Min edge length (mm)	Max edge length (mm)
Iron Core	Triangular	19352	0.19	0.5
Coil		14004	0.18	0.5
Air		256334	0.2	1.0

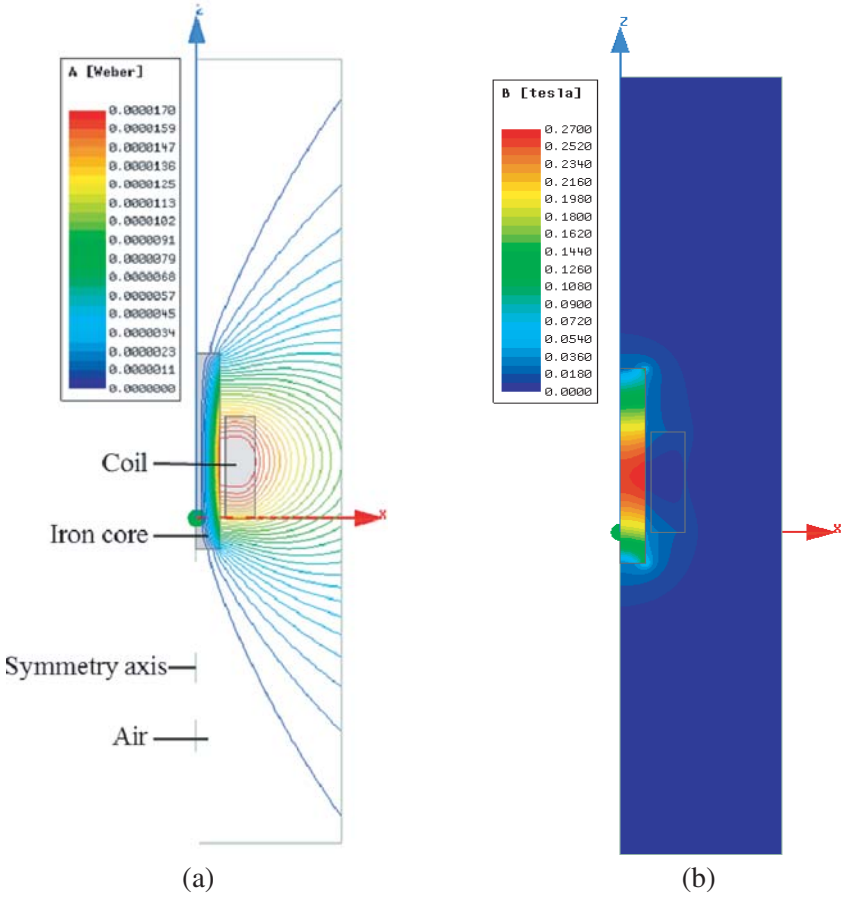

Figure 3. 2D simulation model and magnetic flux. (a) Magnetic flux lines; (b) Magnetic flux density.

the magnetic flux density B_z gradually decreases when the height h_1 increases. It is shown that the magnetic flux density B_z along the radial direction is a positive correlation between the input voltage under the same height h_1 of 5 mm from Fig. 4(b). When the coil assembly voltage is constant and the radial distance e_1 less than about 11 mm, the magnetic flux density B_z changes hardly, which can be explained as that the iron core can concentrate the magnetic field within the radial range of iron core. The magnetic flux density B_z decreases significantly when the radial distance e_1 is greater than 11 mm. Hence, the shape and size of the iron core influence the magnetic field and the drivable area of the coil assembly, which could provide a reference to determine the work positions for micro-robots.

3.2. Electromagnetic Field Measurement

The magnetic flux density B_z along the axial and radial directions of the coil assembly is measured by the Hall sensor to validate the simulated results. The electromagnetic field measurement device is shown in Fig. 5. A XYZ motion system is used to adjust the relative position between the Hall sensor and coil assembly. The power is supplied to the coil through a power amplifier; meanwhile, the voltage

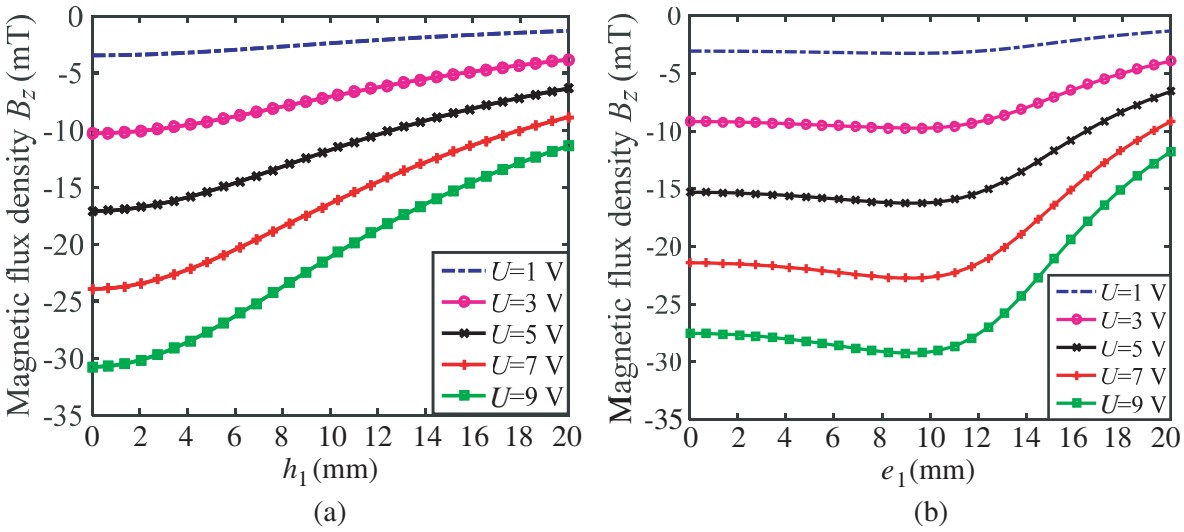

Figure 4. Effect of the voltage U, height h_1, and radial distance e_1 on magnetic flux density B_z. (a) B_z versus h_1 and U, $e_1 = 0$; (b) B_z versus e_1 and U, $h_1 = 5\,\text{mm}$.

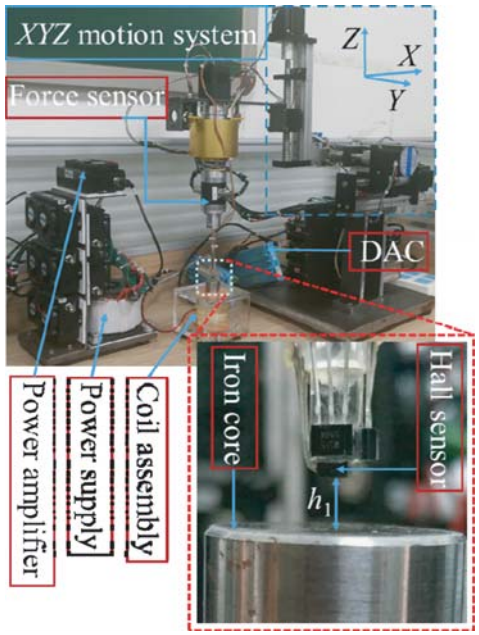

Figure 5. Electromagnetic field measurement device.

command to the coil and measured data acquisition and transmission to the computer are completed by the data acquisition card (DAC). The force sensor is used to measure the magnetic forces in the next section.

The constant voltages of 0, $\pm 4\,\text{V}$, and $\pm 8\,\text{V}$ are applied to the coil assembly through the power supply and power amplifier in the electromagnetic field measurement. The measured magnetic flux density B_z of the coil assembly is compared with the simulated one in Fig. 6. The measured results tend to be consistent with that of simulated ones on the whole. The magnetic field produced by the coil assembly has a good symmetry under the voltage with the same sizes and different directions. According to Fig. 6(a), the magnetic flux density B_z is proportional inversely to the height h_1 but proportional to the input voltage U. However, the measured magnetic flux density B_z is slightly smaller than the

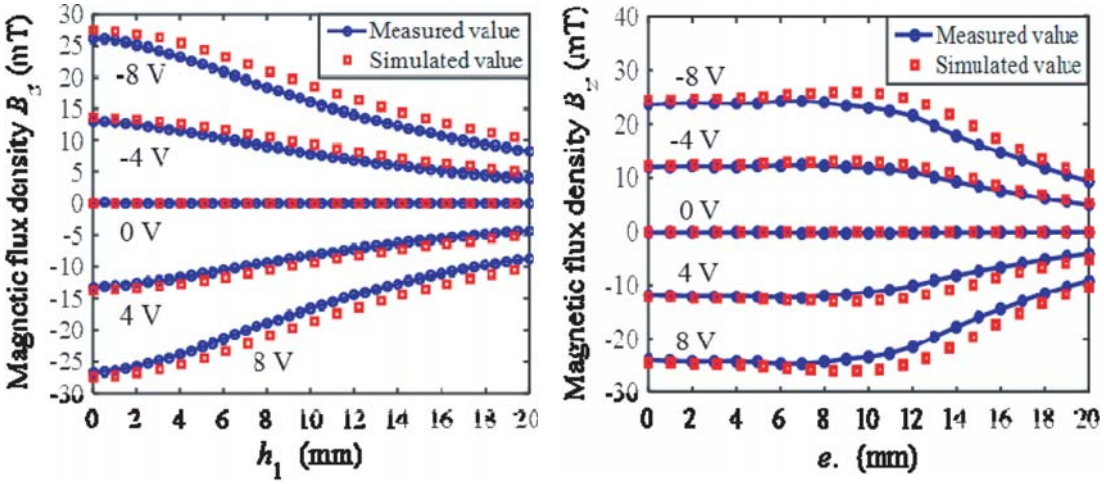

Figure 6. Comparison between the simulated and measured magnetic flux density B_z. (a) B_z versus height h_1 and voltage U, $e_1 = 0$; (b) B_z versus radial distance e_1 and voltage U, $h_1 = 5\,\text{mm}$.

simulated value. It can be explained that it is challenging to keep the measurement probe (Hall sensor) accurately on the coil assembly's central axis during the measuring process. It can be seen from Fig. 6(b) that the magnetic flux density B_z is constant when the radial distance e_1 is less than about 11 mm at a given voltage. The magnetic flux density B_z decreases to zero rapidly when the radial distance e_1 is more than about 11 mm. Meanwhile, the simulated value is a little larger than the measured one. One possible reason is that the actual measurement height h_1 is slightly higher than the ideal height ($h_1 = 5\,\text{mm}$), which causes the measured value decaying faster than the simulated one.

The magnetic field measurement results validate the magnetic field simulation ones. The coil assembly's stability and usability are proved, enabling the development of new electromagnetic actuation systems with improved performance and decreased size. The electromagnetic field for driving micro-robots can be controlled by programming the coil assembly's input voltages or currents. More importantly, in view of the control of a micro-robot movement, it is interesting to learn about the magnetic forces acting on a micro-robot, which is the goal of the following section.

4. SIMULATION AND MEASUREMENT FOR MAGNETIC FORCE

4.1. Theoretical Background

A permanent magnetic micro-cylinder acting as the micro-robot is considered to evaluate the forces acting on the micro-robot. The micro-cylinder is made of NdFeB material; the remanence and relative magnetic permeability are 1 T and 1.1, respectively; the diameter and height are 5 mm. When the magnetized micro-cylinder is exposed to an externally applied electromagnetic field, the interaction between the micro-robot and electromagnetic field gradient generates the magnetic force. The magnetic force acting on the micro-cylinder is defined by the following equation [14, 27]:

$$\mathbf{F} = V(\mathbf{M} \cdot \nabla)\mathbf{B} \tag{1}$$

where $\mathbf{F}$ is the magnetic force, $\mathbf{B}$ a uniform gradient magnetic field, and ∇ a gradient operator. V is the volume of the micro-cylinder, and $\mathbf{M}$ is its magnetization under the assuming of uniform magnetization. The magnetic force acting on the micro-robot is expressed as a function of magnetization $\mathbf{M}$ and magnetic field $\mathbf{B}$ and field gradient. However, there is no analytical expression of the magnetic field generated by the coil with an iron core [30]. Calculating the magnetization is difficult for more complex geometries than ellipsoids [33], and the magnetic force cannot be determined directly. Consequently, the finite element method (FEM) is applied to determine the magnetic force and validated by experimental measurement.

4.2. Magnetic Force Simulation

The magnetic force simulation is also implemented by ANSYS Maxwell. The parameters of the coil assembly are the same as that in Section 3. The model is not axisymmetric when this micro-cylinder is added to the coil assembly. Thus, the three-dimensional simulation is performed to characterize the magnetic forces along the axial and radial directions of the coil assembly. Fig. 7 shows the position relationship between the coil assembly and the micro-cylinder. The upper end and lower end of the micro-cylinder are N pole and S pole, respectively. The magnetization direction of the micro-cylinder is along its central axis. It should be noted that the dimensions are not all scaled to show the fundamental structures clearly in the figure, and the air gap distance is expressed as ap. Fig. 8 shows the mesh of the coil assembly and the micro-cylinder in simulation.

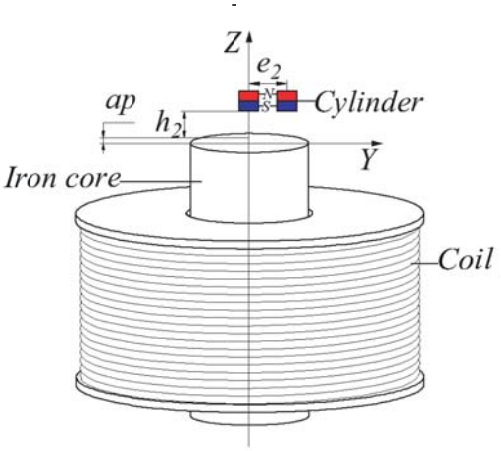

Figure 7. Position relationship between the coil assembly and the micro-cylinder.

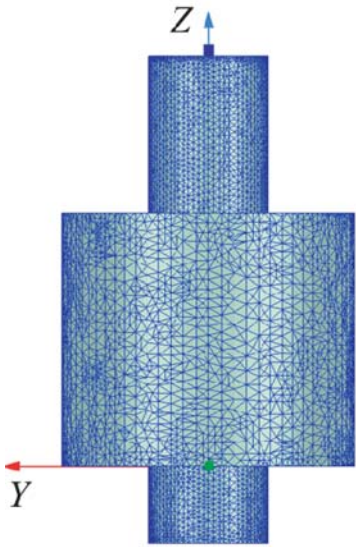

Figure 8. Mesh of the model.

Figure 9 shows the simulated results of magnetic forces at input voltages of the coil of ± 12 V when the micro-cylinder moves along the coil assembly's radial direction. In order to be consistent with the experimental measurement direction, we use F_y to express $-F_y$ here. It can be found that F_x is equal to zero all the way, which results from the symmetry configuration about the Y-axis between

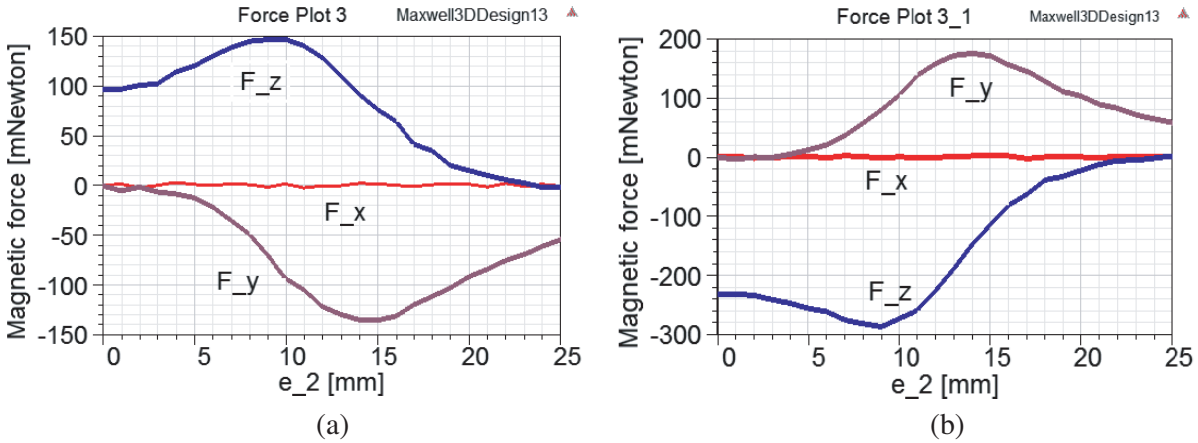

Figure 9. Simulated magnetic forces versus e_2, $h_2 = 5$ mm, $ap = 0$. (a) $U = 12$ V; (b) $U = -12$ V.

the coil assembly and micro-cylinder. F_y and F_z increase and then decrease when radial distance e_2 increases, and their variation gradient gradually increases. However, F_y approaches its maximum value at $e_2 = 14\,\text{mm}$, while F_z gets its maximum value at $e_2 = 9\,\text{mm}$. The other simulated results are indicated and compared with measured ones in the next section.

4.3. Magnetic Force Measurement

As shown in Fig. 5, the force sensor is mounted with the XYZ motion system. The force sensor LZ-SW46 (Provided by Hefei Lizhi Sensor (China) Co., Ltd.) can detect the three-dimensional force information (F_x, F_y, F_z) in Cartesian coordinates simultaneously, and its sensitivity is $0.5 \sim 1.5\,\text{mV/V}$. The micro-cylinder is glued to the tip of a connecting rod with cyanoacrylate glue to measure the magnetic forces applied to this micro-cylinder. The connecting rod is fixed with the force sensor. The arrangement of the force sensor, micro-cylinder, and coil assembly is shown in Fig. 10, which also displays a flowchart for measuring the forces.

A photograph of the micro-cylinder and coil assembly is shown in Fig. 11. The relative position between the coil assembly and micro-cylinder is controlled through the XYZ motion system in

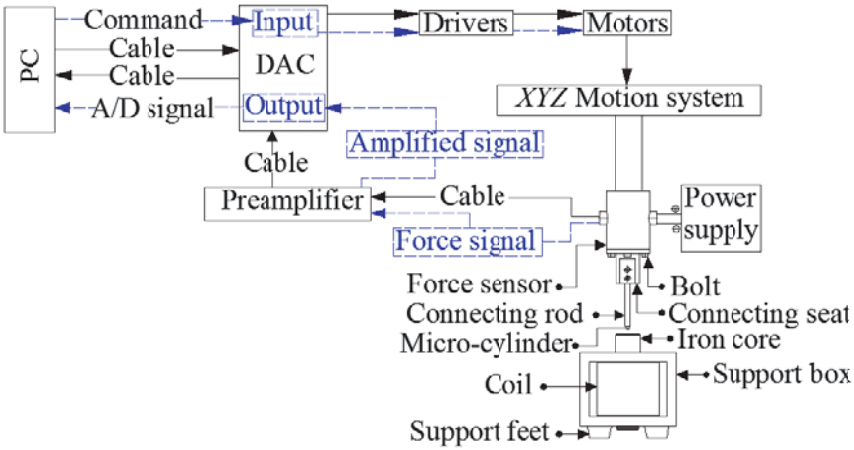

Figure 10. Arrangement of the force sensor, micro-cylinder, and coil assembly; measurement flowchart. Solid line: hardware connection; dotted line: command signal and data transmission.

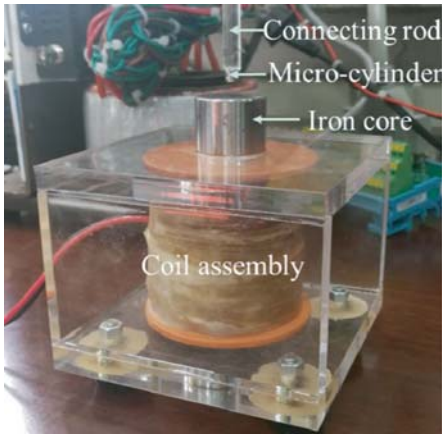

Figure 11. Photograph of the micro-cylinder and coil assembly.

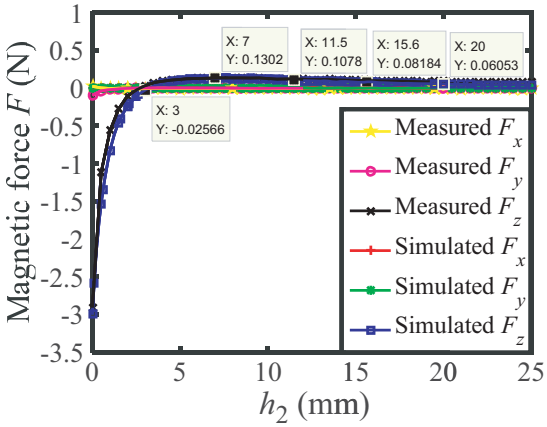

Figure 12. Measured and simulated magnetic forces versus height h_2 ($U = 12\,\text{V}$, $e_2 = 0$, $ap = 0.4\,\text{mm}$).

measurement. A small air gap distance is kept between the micro-cylinder and coil assembly to avoid any contact. The force measuring path includes the axial and radial directions of the coil assembly.

When the micro-cylinder moves along the central axis of the coil assembly, at the input voltage of 12 V, the measured magnetic forces are shown in Fig. 12. The measured results are in good agreement with the simulated ones. The magnetic forces F_x and F_y are tiny and nearly zero compared with the magnetic force F_z, and it can be explained by the symmetry configuration between the micro-cylinder and coil assembly. The magnetic force F_z decreases with the increase of height h_2, but its variation gradient gradually decreases. The magnetic force F_z is less than zero when the height h_2 is less than 3 mm, which indicates that the direction of force F_z is downward. The main reason is the mutual attraction between the micro-cylinder and iron core. The magnetic force F_z is greater than zero when height h_2 is greater than 3 mm, which can be explained by that the interaction between the micro-cylinder and iron core weakens to none with the increase of height h_2. The interaction between the coil magnetic field and micro-cylinder plays a dominant role, leading to a change in force direction due to the same magnetic poles repelling. The magnetic force F_z gradually decreases to zero when height h_2 continues increasing.

Figure 13 indicates the influence of radial distance e_2 on the measured and simulated magnetic forces when the micro-cylinder moves along the coil assembly's radial direction. It also shows that the measured three-dimensional magnetic forces F_x, F_y, and F_z are consistent with the simulated ones on the overall trend no matter the coil assembly's voltage is 10 V or −10 V.

According to Fig. 13, the solid red line with left triangles and solid blue line with right triangles represent the simulated magnetic forces and the measured ones. As shown in Fig. 13(a), F_x keeps nearly

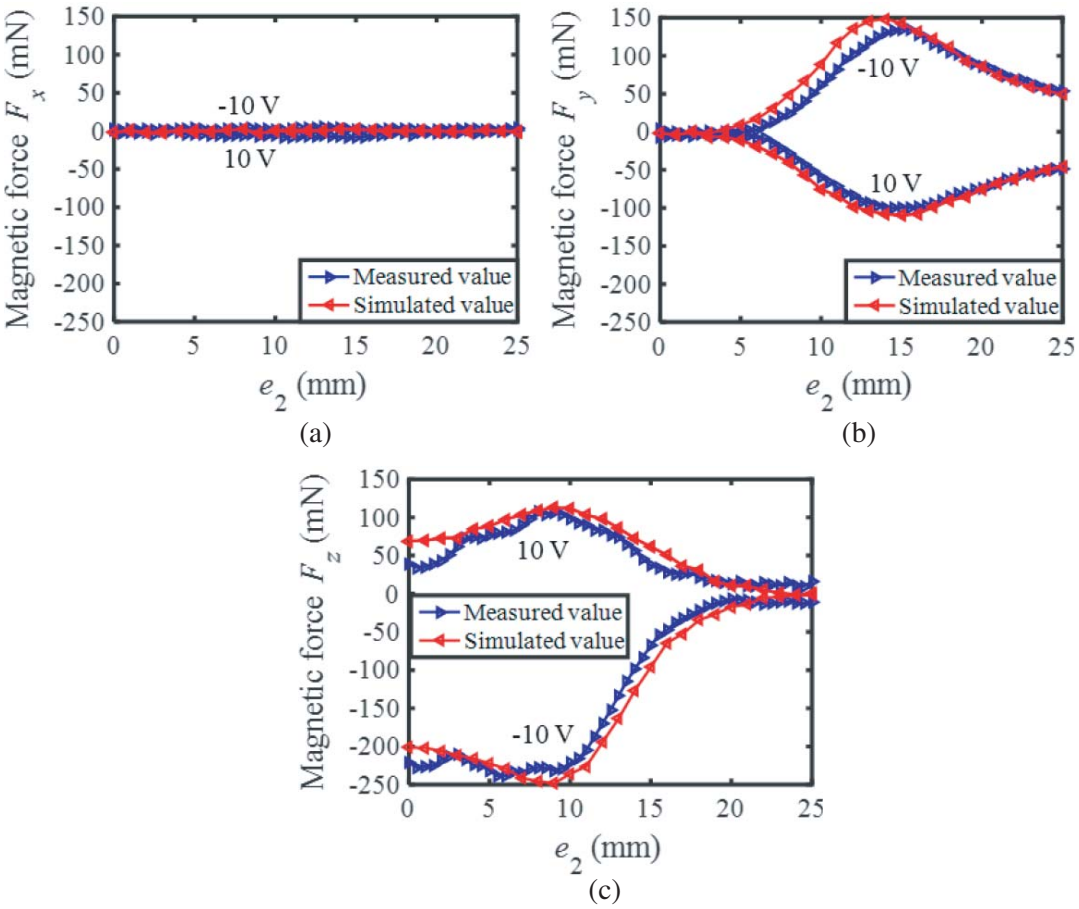

Figure 13. Measured and simulated magnetic forces versus radial distance e_2, $U = \pm 10$ V, $h_2 = 5$ mm, $ap = 0$. (a) F_x versus e_2; (b) F_y versus e_2; (c) F_z versus e_2.

zero and does not vary with voltage U or radial distance e_2 compared with F_y and F_z, which can be explained by the Y-axis symmetry configuration between the micro-cylinder and coil assembly. As we can see in Fig. 13(b), F_y increases firstly and then decreases when the radial distance e_2 increases; correspondingly, its rate of change gradually increases. Fig. 13(c) depicts that the magnetic force F_z increases slightly and decreases when e_2 varies from 0 to 25 mm. Its gradient gradually increases and then decreases whether the voltage of the coil is 10 V or −10 V. It can be explained by Fig. 6(b) that there is a relatively uniform magnetic field within the diameter range of the iron core. After that, the magnetic field decreases evidently when the radial distance e_2 is beyond the iron core range. At the top end of the iron core, the magnetic pole is N pole when the coil assembly's voltage is negative. Now the magnetized iron core is attractive to the micro-cylinder. Thus, the magnetic force F_z is larger under the negative voltage than it under the positive voltage of the coil assembly, so is F_y. However, when the radial distance e_2 is less than about 10 mm, the measured magnetic force F_z fluctuates around the simulated one. On one hand, this can be explained by the minor change of height h_2 in the real experiment progress, because of the intense attraction between micro-cylinder and iron core and the position error of the XYZ motion system. On the other hand, the uneven magnetization of the micro-cylinder is also a potential reason. Both can affect the measured magnetic force F_z.

Another micro-cylinder ($D2 \times 2$ mm) is used to perform the measuring experiments to verify the repeatability and generality of the force measurement. The measurements have been carried out four times with the same input current (1 A) in the coil when the micro-cylinder moves along the coil assembly's central axis (Z-axis). The results are shown in Fig. 14. For each measurement, the maximum value of the three-dimensional forces between micro-cylinder and coil assembly is displayed in Table 3. The force measurement curves trend is consistent with four measurements. The standard deviation

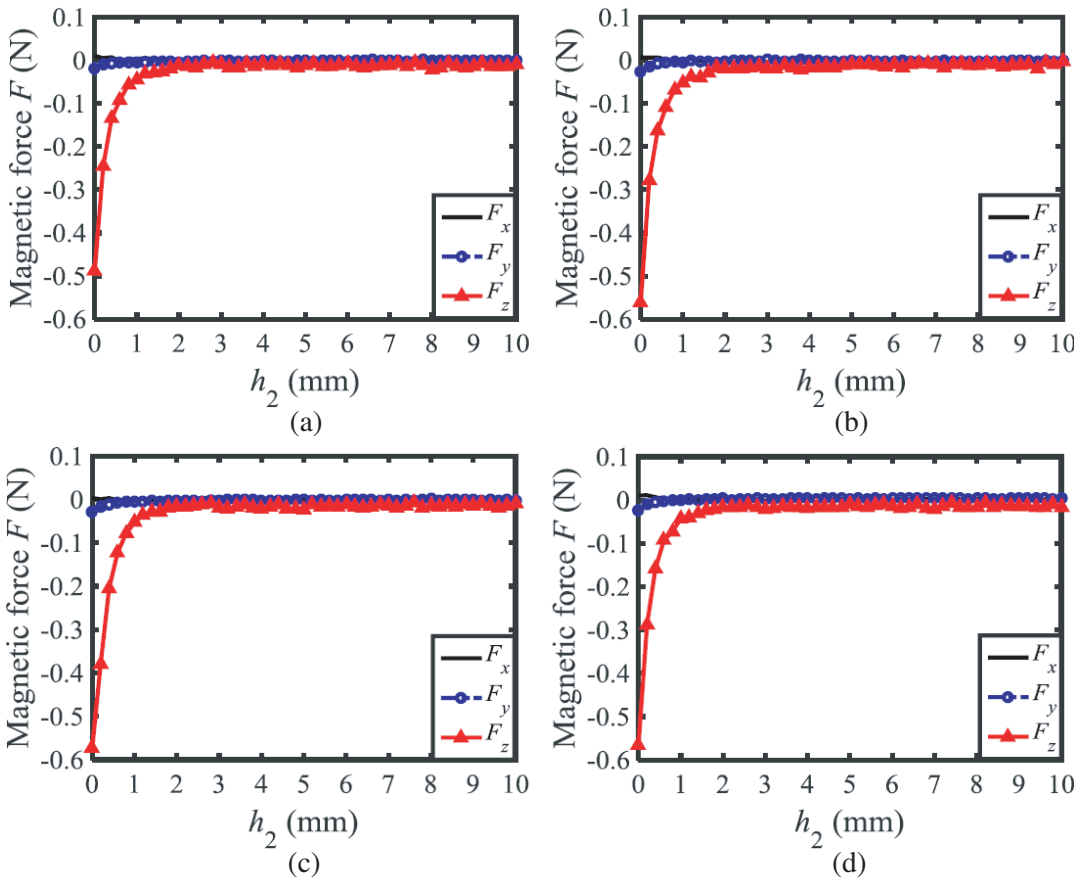

Figure 14. Four measurements of magnetic force at a coil current of 1 A. (a) Measurement 1. (b) Measurement 2. (c) Measurement 3. (d) Measurement 4.

Table 3. Measured maximum force in four measurements ($I = 1\,\mathrm{A}$).

Measurement	Maximum force (N)
1st	−0.4886
2nd	−0.5608
3rd	−0.5740
4th	−0.5654
Average value	−0.5472
Standard deviation	0.0683

of the measured maximum magnetic force is less than 0.07 N, which shows that the magnetic force measurement has good repeatability.

5. CONCLUSION

The following conclusions can be arrived from the above work.

(1) The magnetic field generated by a coil assembly is analyzed by the finite element method with two-dimensional simulation, which has improved the simulation speed (about 5 minutes). Static magnetic force simulation is performed to characterize the magnetic forces acting on a cylindrical permanent magnetic micro-robot in three dimensions.

(2) An affordable experiment measurement device for the magnetic field and force is developed. Both the measured electromagnetic field and forces agree with the simulated ones, demonstrating the simulation's effectiveness. Meanwhile, the repeatability of the force measurement has been confirmed.

(3) The gradient magnetic field can be obtained in the coil assembly's axial direction, and the uniform magnetic field can be obtained in the radial direction within the iron core range. The parameters of relative positions, input voltages or currents, and iron cores influence the electromagnetic field and forces, which could refer researchers to design corresponding electromagnetic driving systems according to different controlled magnetic micro-robots.

In future work, a micro-robot will be driven and controlled by a newly developed electromagnetic driving system composed of five coil assemblies arranged orthogonally.

ACKNOWLEDGMENT

This work was supported by the National Natural Science Foundation of China (NSFC) under grant 51675215, and the Natural Science Foundation of Jilin Province under grant 20170101060JC.

REFERENCES

1. Kim, K., J. Guo, X. Xu, and D. L. Fan, "Recent progress on man-made inorganic nanomachines," *Small*, Vol. 11, No. 33, 4037–4057, 2015.
2. Wang, W., W. Duan, Z. Zhang, M. Sun, A. Sen, and T. E. Mallouk, "A tale of two forces: Simultaneous chemical and acoustic propulsion of bimetallic micromotors," *Chemical Communications*, Vol. 51, No. 6, 1020–1023, 2015.
3. Xu, T., W. Gao, L. P. Xu, X. Zhang, and S. Wang, "Fuel-free synthetic micro-/nanomachines," *Advanced Materials*, Vol. 29, No. 9, 1603250, 2017.
4. Pak, O. S., W. Gao, J. Wang, and E. Lauga, "High-speed propulsion of flexible nanowire motors: Theory and experiments," *Soft Matter*, Vol. 7, No. 18, 8169–8181, 2011.

5. Pawashe, C., S. Floyd, E. Diller, and M. Sitti, "Two-dimensional autonomous microparticle manipulation strategies for magnetic microrobots in fluidic environments," *IEEE Transactions on Robotics*, Vol. 28, No. 2, 467–477, 2012.
6. Fusco, S., M. S. Sakar, S. Kennedy, C. Peters, R. Bottani, F. Starsich, A. Mao, G. A. Sotiriou, S. Pané, S. E. Pratsinis, D. Mooney, and B. J. Nelson, "An integrated microrobotic platform for on-demand, targeted therapeutic interventions," *Advanced Materials*, Vol. 26, No. 6, 952–957, 2014.
7. Nelson, B. J., I. K. Kaliakatsos, and J. J. Abbott, "Microrobots for minimally invasive medicine," *Annual Review of Biomedical Engineering*, Vol. 12, No. 1, 55–85, 2010.
8. Sitti, M., H. Ceylan, W. Hu, J. Giltinan, M. Turan, S. Yim, and E. Diller, "Biomedical Applications of Untethered Mobile Milli/Microrobots," *Proceedings of the IEEE*, Vol. 103, No. 2, 205–224, 2015.
9. Kim, D. I., H. Lee, S. H. Kwon, Y. J. Sung, W. K. Song, and S. Park, "Bilayer hydrogel sheet-type intraocular microrobot for drug delivery and magnetic nanoparticles retrieval," *Advanced Healthcare Materials*, Vol. 9, 2000118, 2020.
10. Xie, M., W. Zhang, C. Fan, C. Wu, Q. Feng, J. Wu, Y. Li, R. Gao, Z. Li, Q. Wang, Y. Cheng, and B. He, "Bioinspired soft microrobots with precise magneto-collective control for microvascular thrombolysis," *Advanced Materials*, Vol. 32, 2000366, 2020.
11. Xie, H., M. Sun, X. Fan, Z. Lin, W. Chen, L. Wang, L. Dong, and Q. He, "Reconfigurable magnetic microrobot swarm: Multimode transformation, locomotion, and manipulation," *Science Robotics*, Vol. 4, No. 28, eaav8006, 2019.
12. He, Y., L. Wang, L. Zhong, Y. Liu, and W. Rong, "Transporting microobjects using a magnetic microrobot at water surfaces," *15th International Conference on Control, Automation, Robotics and Vision ICARCV*, 108–112, 2018.
13. Kim, S. J., G. H. Jang, S. M. Jeon, and J. K. Nam, "A crawling and drilling microrobot driven by an external oscillating or precessional magnetic field in tubular environments," *Journal of Applied Physics*, Vol. 117, 17A703, 2015.
14. Steager, E. B., M. S. Sakar, C. Magee, M. Kennedy, A. Cowley, and V. Kumar, "Automated biomanipulation of single cells using magnetic microrobots," *International Journal of Robotics Research*, Vol. 32, No. 3, 346–359, 2013.
15. Yu, C., J. Kim, H. Choi, J. Choi, S. Jeong, K. Cha, J. O. Park, and S. Park, "Novel electromagnetic actuation system for three-dimensional locomotion and drilling of intravascular microrobot," *Sensors and Actuators, A: Physical*, Vol. 161, No. 1–2, 297–304, 2010.
16. Bouchebout, S., A. Bolopion, J. O. Abrahamians, and S. Régnier, "An overview of multiple DoF magnetic actuated micro-robots," *Journal of Micro-Nano Mechatronics*, Vol. 7, No. 4, 97–113, 2012.
17. Kummer, M. P., J. J. Abbott, B. E. Kratochvil, R. Borer, A. Sengul, and B. J. Nelson, "Octomag: An electromagnetic system for 5-DOF wireless micromanipulation," *IEEE Transactions on Robotics*, Vol. 26, No. 6, 1006–1017, 2010.
18. Byun, D., J. Choi, K. Cha, J. O. Park, and S. Park, "Swimming microrobot actuated by two pairs of Helmholtz coils system," *Mechatronics*, Vol. 21, No. 1, 357–364, 2011.
19. Jeong, S., H. Choi, J. Choi, C. Yu, J. oh Park, and S. Park, "Novel Electromagnetic Actuation (EMA) method for 3-dimensional locomotion of intravascular microrobot," *Sensors and Actuators, A: Physical*, Vol. 157, No. 1, 118–125, 2010.
20. Choi, H., J. Choi, S. Jeong, C. Yu, J. O. Park, and S. Park, "Two-dimensional locomotion of a microrobot with a novel stationary electromagnetic actuation system," *Smart Materials and Structures*, Vol. 18, No. 11, 115017, 2009.
21. Choi, H., J. Choi, G. Jang, J. O. Park, and S. Park, "Two-dimensional actuation of a microrobot with a stationary two-pair coilsystem," *Smart Materials and Structures*, Vol. 18, No. 5, 055007, 2009.
22. Kee, H., H. Lee, H. Choi, and S. Park, "Analysis of drivable area and magnetic force in quadrupole electromagnetic actuation system with movable cores," *Measurement*, Vol. 161, 107878, 2020.

23. Okada, T., S. Guo, N. Xiao, F. Qiang, and Y. Yamauchi, "Control of the wireless microrobot with multi-DOFs locomotion for medical applications," *2012 IEEE International Conference on Mechatronics and Automation ICMA*, 2405–2410, 2012.
24. Li, D., F. Niu, J. Li, X. Li, and D. Sun, "Gradient-enhanced electromagnetic actuation system with a new core shape design for microrobot manipulation," *IEEE Transactions on Industrial Electronics*, Vol. 67, No. 6, 4700–4710, 2020.
25. Ko, Y., S. Na, Y. Lee, K. Cha, S. Y. Ko, J. Park, and S. Park, "A jellyfish-like swimming mini-robot actuated by an electromagnetic actuation system," *Smart Materials and Structures*, Vol. 21, No. 5, 057001, 2012.
26. Fu, Q., S. Guo, and J. Guo, "Conceptual design of a novel magnetically actuated hybrid microrobot," *2017 IEEE International Conference on Mechatronics and Automation, ICMA*, 1001–1005, 2017.
27. Yesin, K. B., K. Vollmers, and B. J. Nelson, "Modeling and control of untethered biomicrorobots in a fluidic environment using electromagnetic fields," *International Journal of Robotics Research*, Vol. 25, No. 5–6, 527–536, 2006.
28. Shiri, A. and A. Shoulaie, "A new methodology for magnetic force calculations between planar spiral coils," *Progress In Electromagnetics Research*, Vol. 95, 39–57, 2009.
29. Marino, H., C. Bergeles, and B. J. Nelson, "Robust electromagnetic control of microrobots under force and localization uncertainties," *IEEE Transactions on Automation Science and Engineering*, Vol. 11, No. 1, 310–316, 2014.
30. Wang, L. F., M. Dkhil, A. Bolopion, P. Rougeot, S. Regnier, and M. Gauthier, "Simulation and experiments on magnetic microforces for magnetic microrobots applications," *2013 International Conference on Manipulation, Manufacturing and Measurement on the Nanoscale 3M-NANO*, 15–20, 2013.
31. Ivan, I. A., G. Hwang, J. Agnus, and M. Rakotondrabe, "First experiments on MagPieR: A planar wireless magnetic and piezoelectric microrobot," *2011 IEEE International Conference on Robotics and Automation Shanghai International Conference Center*, 102–108, 2011.
32. Keuning, J. D., J. D. Vriesy, L. Abelmanny, and S. Misra, "Image-based magnetic control of paramagnetic microparticles in water," *2011 IEEE/RSJ International Conference on Intelligent Robots and Systems*, 421–426, 2011.
33. Beleggia, M., M. D. Graef, and Y. T. Millev, "The equivalent ellipsoid of a magnetized body," *Journal of Physics D: Applied Physics*, Vol. 39, No. 5, 891–899, 2006.